

# Simulations of seismic wave propagation using a spectral-element method in a Lagrangian framework with logarithmic strain

Uno Vaaland,<sup>1</sup> Hom Nath Gharti<sup>2</sup> and Jeroen Tromp<sup>1,2</sup>

<sup>1</sup>Program in Applied & Computational Mathematics, Princeton University, Princeton, NJ 08544, USA. E-mail: [uvaaland@princeton.edu](mailto:uvaaland@princeton.edu)

<sup>2</sup>Department of Geosciences, Princeton University, Princeton, NJ 08544, USA

Accepted 2018 November 28. Received 2018 November 26; in original form 2018 September 21

## SUMMARY

We show how the linearized equations that govern the motion of a body that undergoes deformation can be generalized to capture geometrical non-linearities in a spectral-element formulation. Generalizing the equations adds little complexity, the main addition being that we have to track the deformation gradient. Geometrical changes due to deformation are captured using the logarithmic strain. We test the geometrically non-linear formulation by considering numerical experiments in seismic wave propagation and cantilever beam bending and compare the results with the linearized formulation. In cases where finite deformation occurs, the effect of solving the geometrically non-linear equations can be significant while in cases where deformation is smaller the result is similar to solving the linearized equations. We find that the time it takes to run the geometrically non-linear simulations is on the same order of magnitude as running the linearized simulations. The limited amount of added cost and complexity suggests that we might as well solve the geometrically non-linear equations since it does not assume anything about the size of deformations.

**Key words:** Numerical modelling; Computational seismology; Wave propagation.

## 1 INTRODUCTION

In seismological simulations the governing equations are commonly linearized, which simplifies the formulation and makes it easier to optimize the computation cost. Since the deformations are often small, the strictly linearized formulation is a good approximation to real world observations (Dahlen & Tromp 1998, p. 56). In certain cases, however, deformations can be large and a more general approach is needed. Finite deformation occurs when a solid is deformed such that the undeformed and the deformed shapes are significantly different. Under these conditions the governing equations cannot be linearized and we have to consider non-linear effects (Zienkiewicz *et al.* 2014). Non-linear behaviour in solids can involve both material non-linearities and geometrical non-linearities (Novozhilov 1999; Zienkiewicz *et al.* 2014). By material non-linearities we mean non-linear effects in the constitutive relationship that ties stresses to strains in a body. Geometrical non-linearities are non-linear effects associated with how the geometry of a body changes as it deforms, and this involves working with a non-linear strain measure. In the classical, linearized formulation, the material is described by Hooke's law, while the geometrical descriptions hinges on the assumption that deformations are infinitesimal, such that the infinitesimal strain measure can be used. However, it is known that deformations can be large in the near-field (Aki 1968; Heaton 1990). Furthermore, laboratory tests in the 1970s (Hardin & Drnevich 1972), and downhole investigations,

such as the Lotung Large-Scale Seismic Test (LSST; Elgamal *et al.* 1995; Zeghal *et al.* 1995; Chang *et al.* 1996), found evidence of non-linear material behaviour in soft sediments and soils. This has been the focus of many works that have looked at soil amplification in weak and strong motion (Aki 1993; Beresnev & Wen 1996; Field *et al.* 1997; Ichimura *et al.* 2015). In such cases, non-linear effects are observed as sediments begin to yield beyond a certain level of strain. This type of behaviour violates the classical assumptions and suggests that a more sophisticated description of the material and geometry is needed in order to accurately incorporate these non-linear effects (Field *et al.* 1998; Pavlenko 2001).

Our aim in this paper is not to provide a complete generalization of the governing equations, but to show how the classical formulation, in the weak form, can be extended to a geometrically non-linear formulation with only minor modifications. This means that our model can deal with deformations of any size, but it uses Hooke's law as the constitutive relation, which means that there is a linear relationship between the applied stresses and a logarithmic strain measure. With the geometrical effects accounted for, we are well positioned to further extend the model and explore alternative constitutive relationships that capture non-linear material behaviour.

In the weak form, the equation of motion can be generalized to a geometrically non-linear form that is analogous to the weak form of the linearized equation of motion. This is accomplished by formulating the governing equations in a Lagrangian framework, also known as the 'total Lagrangian' (Wood & Zienkiewicz 1977;

Miller *et al.* 2007), and by introducing a logarithmic strain measure (Hencky 1928; Tarantola 2005) into the formulation. The only added complexity is that we need to track the deformation gradient. Therefore, given a finite- or spectral-element (Komatitsch & Vilotte 1998) implementation of the linearized equations, only minor modifications to the code are necessary in order to achieve an implementation that captures geometrical non-linearities. We implement the geometrically non-linear formulation by using SPECFEM3D Cartesian (Komatitsch & Tromp 2002a,b; Peter *et al.* 2011; Komatitsch *et al.* 2012) 2.0.2 published under the GPL 2 license. Numerical examples in seismic wave propagation and cantilever beam bending are considered. The former being a case where the deformations are commonly small, and the latter a case where finite deformations are expected to occur.

In this work our focus is strictly on geometrical non-linearities and we do not consider any non-linear effects tied to the material description. For geometrically non-linear problems the strain in a body cannot be represented by a linear measure, so we must consider a more general measure, such as the logarithmic strain. We use a spectral-element method to solve our problem, which is a flavour of the finite-element method where discretization on the element is accomplished with high-degree Lagrange interpolants and integration on an element is achieved with Gauss–Lobatto–Legendre (GLL) quadrature. Using this type of discretization and integration together leads to a diagonal mass matrix, which greatly simplifies the algorithm (Komatitsch & Tromp 1999). Two approaches are commonly considered when solving geometrically non-linear problems with a finite-element approximation. The discrete equations can be formulated with respect to the reference configuration in what is called the ‘total Lagrangian’ approach, or they can be written with respect to the current configuration, which is called the ‘updated Lagrangian’ approach. In this work we take the total Lagrangian approach, which has the advantage that the initial configuration remains constant, thereby simplifying the formulation and computation (Wood & Zienkiewicz 1977).

The purpose of this paper is to show how elegantly the linearized governing equations in the weak form can be generalized to capture geometrical non-linearities. The small amount of added complexity and cost suggests that we might as well solve the geometrically non-linear equations. The numerical examples are meant to explore the effects of using the more general formulation.

Throughout this paper we use as much as possible the notation that lowercase letters and indices refer to quantities in the current configuration (e.g.  $x^i$ ), and upper case letters and indices to quantities in the reference configuration (e.g.  $X^i$ ). Partial derivatives with respect to  $x^i$  and  $X^i$  are denoted by  $\partial_i$  and  $\partial_I$ , respectively. We use the terms ‘Eulerian’ and ‘Lagrangian’ in the classical sense, where ‘Eulerian’ refers to specific locations in space in the current configuration and ‘Lagrangian’ refers to specific material points in the continuum in the reference configuration. We use  $\Omega^0$  and  $\partial\Omega^0$  to refer to the domain and boundary of a continuum in the reference configuration, and  $\Omega$  and  $\partial\Omega$  for the same quantities in the current configuration. Finally, we refer to the governing equations in their geometrically non-linear form as the ‘general equations’, and in their classical, linearized form as the ‘classical equations’.

## 2 FORMULATION

We seek a description of the motion of a body that undergoes finite deformation. Let  $E \in \mathbb{R}^3$  be Cartesian and consider a body  $B \subseteq E$  whose physical quantities are differentiable almost everywhere. The

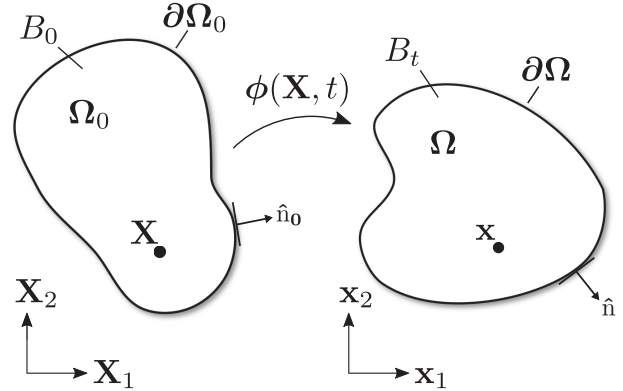


**Figure 1.** A body  $B \subseteq E \in \mathbb{R}^3$  subject to finite deformation as it moves through space. The figure shows the initial configuration of the body,  $B_0$ , on the left, and the current configuration,  $B_t$ , on the right. Points in the initial configuration,  $X$ , are called material points, and points in the current configuration,  $x$ , are called spatial points.  $\phi$  is a mapping function that maps material points in the initial configuration to the corresponding spatial points in the current configuration. The domain, boundary and boundary normal in the current configuration are denoted by  $\Omega$ ,  $\partial\Omega$  and  $\hat{n}$ , respectively. A subscript zero is used for the same quantities in the initial configuration.

region occupied by  $B$  at time  $t$  is called the configuration of  $B$  at time  $t$ , denoted  $B_t$ , and we refer to the configuration of  $B$  at some initial time  $t_0$  as the reference configuration,  $B_0$ . We call points  $x \in B_t$  spatial points, with Cartesian coordinates  $(x^1, x^2, x^3)$ . Points  $X \in B_0$  are called material points and have Cartesian coordinates  $(X^1, X^2, X^3)$  in the reference configuration. Fig. 1 shows the relevant setup where a body  $B$  has a domain  $\Omega_0$  with boundary  $\partial\Omega_0$  and boundary normal  $\hat{n}_0$  in the reference configuration,  $B_0$ . At some later time,  $t$ , the body has been deformed and it now has a domain  $\Omega$  with boundary  $\partial\Omega$  and boundary normal  $\hat{n}$  in the current configuration,  $B_t$ . The motion of  $B$  is determined by a mapping  $\phi: B_0 \rightarrow B_t$  of the form

$$x^i = \phi^i(X, t), \quad (1)$$

which returns the spatial coordinates,  $\{x^i\}$ , of a material point,  $\{X^i\}$ , at a given time,  $t$ . This concept is similar to the notion of displacement, that is we could write

$$x^i = \delta_I^i X^I + s^i(X, t), \quad (2)$$

where  $\delta$  denotes the Kronecker delta and  $s^i$  the displacement field, such that if  $s^i(X, 0) = 0$ , then the two coordinate systems coincide at time  $t = 0$ .

In tracking the motion of a body  $B$  that undergoes finite deformation, we can choose to employ either the Eulerian or the Lagrangian description of motion. In the Eulerian description, the motion is described by monitoring fixed spatial points,  $x \in B_t$ , while in the Lagrangian description, the motion is described by tracking material points,  $X \in B_0$ . Both descriptions capture the motion of  $B$  completely. Every scalar, vector, or tensor quantity in  $B$  has both an Eulerian description and a Lagrangian description. Given a quantity (a scalar, vector or tensor) with Eulerian description  $q(x, t)$  and Lagrangian description  $Q(X, t)$ , the two descriptions are related via (Dahlen & Tromp 1998, eq. 2.1)

$$q(\phi(X, t), t) = Q(X, t). \quad (3)$$

That is, the Eulerian quantity  $q$  that is tracking the spatial location of some material point  $X$  is equal to the Lagrangian quantity  $Q$ . If the deformation of  $B$  is sufficiently small, the governing

equations can be linearized, and the distinction between the Eulerian and Lagrangian descriptions becomes immaterial. If, however, the deformation of  $B$  is finite, the governing equations must be solved in their general form and then it is necessary to distinguish between the Eulerian and the Lagrangian descriptions of motion.

## 2.1 Equations of motion

The motion of a body  $B$  that undergoes deformation is captured by the equations of motion. Let  $\rho$  denote mass density,  $\mathbf{v}$  material velocity,  $\mathbf{t}$  the Cauchy stress tensor, and  $\mathbf{f}$  a body force. Then conservation of mass, linear momentum and angular momentum can be expressed as, respectively,

$$\mathbf{D}_t \rho + \rho \nabla \cdot \mathbf{v} = 0, \quad (4)$$

$$\rho \mathbf{D}_t \mathbf{v} = \nabla \cdot \mathbf{t} + \mathbf{f}, \quad (5)$$

$$\mathbf{t}^T = \mathbf{t}, \quad (6)$$

where a superscript  $T$  denotes the transpose, and  $\mathbf{D}_t$  denotes the Lagrangian (material) time derivative, which is related to the Eulerian (spatial) time derivative,  $\mathbf{d}_t$ , via

$$\mathbf{D}_t = \mathbf{d}_t + \mathbf{v} \cdot \nabla. \quad (7)$$

In the following sections we formulate the equations of motion in the Eulerian and Lagrangian descriptions.

## 2.2 Eulerian description

In the Eulerian description, the motion is described in terms of spatial points  $x \in B_t$  with Cartesian coordinates  $(x^1, x^2, x^3)$ . In this description the conservation laws (4)–(6) become

$$\partial_t \rho + \partial_i(\rho v^i) = 0, \quad (8)$$

$$\rho (\partial_t v^i + v^j \partial_j v^i) = \partial_j t^{ji} + \rho g^i, \quad (9)$$

$$t^{ji} = t^{ij}, \quad (10)$$

where the Einstein summation convention is implied, and  $g^i$  is the specific body force per unit mass. Note that the Cartesian Eulerian components of vectors and tensors depend on the Cartesian Eulerian coordinates and time, for example  $v^i(x, t)$  and  $t^{ij}(x, t)$ .

The deformation that  $B$  undergoes is governed by the momentum eq. (9). We can rewrite this equation in terms of its weak form as follows:

$$\int_{\Omega} \rho w_i (\partial_t v^i + v^j \partial_j v^i) d^3x = \int_{\partial\Omega} \hat{n}_j t^{ji} w_i d^2x - \int_{\Omega} t^{ji} \partial_j w_i d^3x + \int_{\Omega} \rho g^i w_i d^3x, \quad (11)$$

where  $w_i$  denotes the elements of a test vector (strictly speaking a one-form), and  $\Omega$  the model domain with boundary  $\partial\Omega$ . On a stress free boundary the traction  $\hat{n}_j t^{ji}$  vanishes, in which case the surface integral is zero.

For small deformations, we may linearize the weak form (11) and rewrite it in terms of displacement as

$$\begin{aligned} \int_{\Omega} \rho w_i \partial_t^2 s^i d^3x &= \int_{\partial\Omega} \hat{n}_j t^{ji} w_i d^2x - \int_{\Omega} t^{ji} \partial_j w_i d^3x \\ &+ \int_{\Omega} \rho g^i w_i d^3x. \end{aligned} \quad (12)$$

This is the weak form that the SPECFEM3D Cartesian solver (Komatsitsch & Tromp 2002a,b; Peter *et al.* 2011; Komatsitsch *et al.* 2012) implements for a Hookean rheology. In this linearized version of the equation of conservation of linear momentum, Eulerian and Lagrangian coordinates are equivalent.

## 2.3 Lagrangian description

In the Lagrangian description, the motion is described in terms of material points  $X \in B_0$  with Cartesian coordinates  $(X^1, X^2, X^3)$ . In order to express the conservation laws (4)–(6) in the Lagrangian description, we need to make a change from Eulerian to Lagrangian coordinates. Using eq. (3), we define the Lagrangian variables

$$R(X, t) \equiv \rho(\phi(X, t), t), \quad (13)$$

$$V^i(X, t) \equiv v^i(\phi(X, t), t), \quad (14)$$

$$G^i(X, t) \equiv g^i(\phi(X, t), t). \quad (15)$$

The Lagrangian velocity may also be expressed in terms of the displacement field by using eqs (1) and (2)

$$V^i(X, t) \equiv \partial_t \phi^i(X, t) = \partial_t s^i(X, t), \quad (16)$$

which allows us to write

$$\begin{aligned} \rho (\partial_t v^i + v^j \partial_j v^i) &= R \partial_t V^i \\ &= R \partial_t^2 \phi^i \\ &= R \partial_t s^i. \end{aligned} \quad (17)$$

Note that the mapping function  $\phi$  is a function of two variables, namely, the material point  $X$  and time  $t$ . Taking the partial derivative with respect to time gives us the particle velocity, as shown in (16). The other partial derivative, with respect to the material point, gives us the deformation gradient, which is needed when going from Eulerian to Lagrangian coordinates:

$$F^i{}_I(X, t) \equiv \partial_I \phi^i(X, t) = \delta_I^i + \partial_I s^i(X, t), \quad (18)$$

The deformation gradient describes the local deformation at a material point  $X$ . It is often called a two-point tensor because one index is tied to the reference configuration, while the other index is tied to the current configuration. Taking the determinant of the deformation gradient, we obtain the Jacobian

$$J = \det(F^i{}_I). \quad (19)$$

A volume element changes according to

$$d^3x = J(X, t) d^3X. \quad (20)$$

Similarly, a surface element changes according to (Dahlen & Tromp 1998, eq. 2.37)

$$\hat{n}_i d^2x = J \hat{n}_I^0 (F^{-1})^I{}_i d^2X. \quad (21)$$

With a change to Lagrangian coordinates, the conservation laws become (Dahlen & Tromp 1998, eqs 2.86, 2.93, 2.94, 2.96)

$$R(X, t) J(X, t) = R_0(X), \quad (22)$$

$$\begin{aligned} R_0 \partial_t^2 s^i &= \partial_J (S^{JI} F^I{}_J) + R_0 G^i \\ &= \partial_J P^{JI} + R_0 G^i, \end{aligned} \quad (23)$$

$$S^{JI} = S^{IJ}. \quad (24)$$

Here  $S^{IJ}$  are the components of the second Piola–Kirchhoff stress, which are related to the components of the Cauchy stress via (Dahlen & Tromp 1998, eq. 2.46)

$$t^{ij} = J^{-1} F^i{}_I S^{IJ} F^J{}_j, \quad (25)$$

and  $P^{JI}$  are the components of the first Piola–Kirchhoff stress, which are related to the components of the second Piola–Kirchhoff and Cauchy stresses via (Dahlen & Tromp 1998, eq. 2.45)

$$P^{JI} = S^{IJ} F^i{}_J = J (F^{-1})^I{}_j t^{ji}. \quad (26)$$

The Lagrangian description of the weak form of the momentum equation can be obtained by using eqs (17), (18), (22) and (25) in eq. (11), which yields

$$\begin{aligned} \int_{\Omega^0} R_0 W_i \partial_t^2 s^i d^3 X &= \int_{\partial\Omega^0} \hat{n}_J^0 S^{JI} F^i{}_I W_i d^2 X \\ &\quad - \int_{\Omega^0} S^{JI} F^i{}_I \partial_J W_i d^3 X \\ &\quad + \int_{\Omega^0} R_0 G^i W_i d^3 X, \end{aligned} \quad (27)$$

where  $\Omega^0$  denotes the reference volume with surface  $\partial\Omega^0$ . Alternatively, in terms of the first Piola–Kirchhoff stress we have

$$\begin{aligned} \int_{\Omega^0} R_0 W_i \partial_t^2 s^i d^3 X &= \int_{\partial\Omega^0} \hat{n}_J^0 P^{JI} W_i d^2 X - \int_{\Omega^0} P^{JI} \partial_J W_i d^3 X \\ &\quad + \int_{\Omega^0} R_0 G^i W_i d^3 X. \end{aligned} \quad (28)$$

Written in terms of the first Piola–Kirchhoff stress, we can see that eq. (28) is term-by-term analogous to the weak form for the classical linearized theory in (12). The key differences are that this exact form of conservation of linear momentum is expressed using the first Piola–Kirchhoff stress instead of the Cauchy stress, and that the integrals are evaluated in the reference configuration. However, going from the first Piola–Kirchhoff stress to the Cauchy stress and from any configuration of  $B$  to the reference configuration only requires the deformation gradient (18), as shown by eqs (19), (20), (21), (22) and (26). As in the Eulerian case, on a stress free boundary the surface integral vanishes.

From a computational perspective, spectral-element software currently using eq. (12), for example SPECFEM3D, can just as easily be used to solve the exact Lagrangian weak form of conservation of linear momentum (28). To accomplish this, the mesher should be regarded as providing a mesh of the reference domain  $\Omega_0$ . The solver needs to use the first Piola–Kirchhoff stress rather than the Cauchy stress, but the deformation gradient,  $F^I_I$  and its Jacobian,  $J$ , required for the related transformation are already available, because the displacement gradient,  $\partial_I s^i$ , is needed to calculate the infinitesimal strain. Thus, implementation of a spectral-element solver in the exact Lagrangian framework is just as simple as its implementation in the linearized framework.

## 2.4 Logarithmic strain

When deformations are small we can use the infinitesimal strain measure to represent strain in a body. For large deformations, however, we must use a more sophisticated strain measure that captures non-linear geometrical changes. There are several non-linear strain measures to choose from, for example the Lagrangian strain or the Eulerian strain, but for this work we will use the logarithmic, or Hencky, strain (Hencky 1928; Tarantola 2005), which is a more general strain measure than the aforementioned Lagrangian and Eulerian strain measures. The Eulerian elements of the logarithmic strain tensor are defined as

$$e^i{}_j \equiv \frac{1}{2} (\log b)^i{}_j, \quad (29)$$

where  $b^i{}_j$  denotes the elements of the left Cauchy–Green tensor

$$b^i{}_j \equiv F^i{}_I (F^I)^j{}_j. \quad (30)$$

Eq. (29) can be expressed as a power series, namely,

$$\begin{aligned} e^i{}_j &\equiv \frac{1}{2} (\log b)^i{}_j \approx \frac{1}{2} (b^i{}_j - \delta^i{}_j) \\ &\quad - \frac{1}{4} (b^k{}_k - \delta^k{}_k)(b^l{}_l - \delta^l{}_l) + \dots \end{aligned} \quad (31)$$

where  $\delta$  is the Kronecker delta. Truncating the power series after the first order term leads to

$$E^i{}_j = \frac{1}{2} (b - \delta)^i{}_j, \quad (32)$$

which is commonly referred to as the Lagrangian strain (Dahlen & Tromp 1998, eq. 3.113). In the linear approximation, where the distinction between Eulerian and Lagrangian coordinates becomes irrelevant, the logarithmic and Lagrangian strain reduce to the familiar infinitesimal strain measure

$$\varepsilon_{ij} = \frac{1}{2} (\partial_j s_i + \partial_i s_j). \quad (33)$$

Given the deformation gradient (18), the Eulerian logarithmic strain can be computed from the left Cauchy–Green tensor based on the power series expansion (31). The power series may be terminated once the additional terms fall below a set threshold.

## 2.5 Constitutive relation

In order to complete the formulation of the governing equations it is necessary to describe how the material behaves when it undergoes deformation. This is governed by the constitutive relation. In this study, we consider the material to be isotropic and linearly elastic, meaning the stress and strain tensors are linearly related according to Hooke's law. In an isotropic medium, Hooke's law is given by

$$t^i{}_j = \kappa e_k^k \delta^i{}_j + 2 \mu (e^i{}_j - \frac{1}{3} e^k{}_k \delta^i{}_j), \quad (34)$$

where  $\kappa$  denotes the bulk modulus and  $\mu$  the shear modulus of the medium. This equation can be rewritten in terms of the first Piola–Kirchhoff stress by using (26)<sup>1</sup>

$$\begin{aligned} P^{II} &= J (F^{-1})^I{}_j t^{ji} \\ &= (F^{-1})^I{}_j [\kappa_0 e^k{}_k \delta^{II} + 2 \mu^0 (e^{II} - \frac{1}{3} e^k{}_k \delta^{II})], \end{aligned} \quad (35)$$

where

$$\kappa^0(X) = J(X, t) \kappa(X, t), \quad (36)$$

<sup>1</sup>Note that raising and lowering indices is accomplished with the Cartesian metric tensor (either in Eulerian or Lagrangian coordinates), that is  $g_{ij} = \delta_{ij}$  &  $g^{ij} = \delta^{ij}$  &  $G_{IJ} = \delta_{IJ}$  &  $G^{IJ} = \delta^{IJ}$ , so this may be done at will.

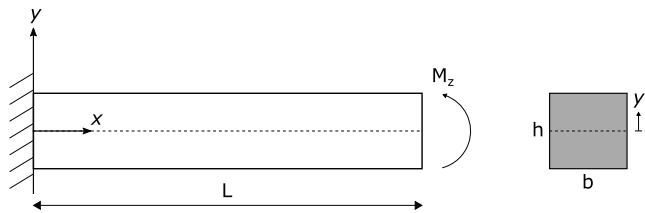


**Figure 2.** Schematic diagram of the cantilever beam experiment setup. The neutral axis is shown as a dashed line.

$$\mu^0(X) = J(X, t) \mu(X, t), \quad (37)$$

similar to conservation of mass (22). As a result, we only need the model parameters  $\rho^0, \kappa^0$  and  $\mu^0$ , that is, the model parameters in the reference configuration. Eqs (28), (29) and (35), together with specific initial and boundary conditions, constitute the geometrically non-linear governing equations that we solve numerically using a spectral-element method.

We reiterate that our focus in this paper is to show how the classical formulation of the governing equations, in the weak form, can be extended to a geometrically non-linear formulation with only minor modifications. Therefore, we restrict our scope to a material description, Hooke's law, which here provides a linear relationship between the applied stresses and a logarithmic strain measure. With the geometrically non-linear formulation in place, however, we are free to consider other material descriptions that account for material non-linear effects to further generalize the formulation.

### 3 NUMERICAL EXAMPLES

In order to study the effects of solving the geometrically non-linear equations, we consider two numerical experiments. In the first experiment we study finite bending of an elastic cantilever beam. We record the deflection of the beam and compare the result with the classical, linearized theory. The second experiment is a seismic experiment where we study wave propagation in two different elastic models with two different source configurations. We record the displacement field in the entire model and compare it with the classical theory, that is the linear approximation.

#### 3.1 Cantilever beam experiment

For finite bending of an isotropic elastic cantilever beam, we consider the setup shown in Fig. 2. The beam is oriented such that the length of the beam is parallel to the  $x$ -axis, its height runs along the  $y$ -axis, and the breadth of the beam is parallel to the  $z$ -axis, with an origin in the center of the beam. The beam is  $L = 10.0$  m long,  $h = 0.02$  m tall and  $b = 0.02$  m wide. This gives the beam a  $L/h$  ratio of 500, making it suitable for Euler–Bernoulli beam theory (Zienkiewicz *et al.* 2013, p. 439). The beam has Young's modulus  $E = 13.4$  GPa and Poisson's ratio  $\nu = 0.30$ . The boundary conditions are such that the beam is fixed at  $x = 0$ , and an external traction is applied on the free end at  $x = L$ . Specifically, the boundary term in the Lagrangian weak form (28) involves the traction

$$\hat{n}_j^0 P^{Ji} = J \hat{n}_j^0 (F^{-1})_j^J \tilde{\tau}^{ji}, \quad \text{on } \partial\Omega_0, \quad (38)$$

where the only non-zero element of  $\tilde{\tau}^{ji}$  is

$$\tilde{\tau}^{11} = -\frac{M_z}{I_{xx}} y. \quad (39)$$

Here  $M_z$  is the moment about the  $z$ -axis,  $I_{xx}$  the second moment of area, and  $y$  the perpendicular distance to the  $x$ -axis.

The mesh consists of 500 spectral elements and we use 5 GLL points in each direction, which gives a total of 50 500 degrees of freedom. The mesh is uniform with element size 0.02 m. For the quasi-static simulation we use a timestep of  $\Delta t = 0.5 \mu\text{m}$  and we run the simulation for 100 s. For the dynamic simulation we use the same timestep and run the simulation for 25 s. We record the  $y$ -component of the displacement (deflection), for every time step, along the neutral axis of the beam ( $y = 0$ ).

In order to ensure correctness of the implementation of the cantilever beam experiment, we benchmark the SPECFEM implementation of the classical theory with Euler–Bernoulli beam theory. We consider two benchmarks. In the first benchmark we compare our implementation with the Euler–Bernoulli solution to the static beam equation. In the second benchmark we compare our implementation with the Euler–Bernoulli solution to the dynamic beam equation for two cases: (i) starting from the first mode solution and (ii) starting from the static solution.

Using Euler–Bernoulli theory together with Hooke's law for an isotropic material, we can express the deflection of a cantilever beam as (e.g. Gere & Goodno 2008)

$$s_y = \frac{M_z x^2}{2 E I_{xx}}, \quad (40)$$

where  $s_y$  is the deflection and  $E$  is Young's modulus. Fig. 3(a) shows this analytical solution plotted together with the classical SPECFEM implementation.

The Euler–Bernoulli solution to the dynamic beam equation may be expressed in terms of harmonic modes as (Bottega 2006)

$$s_y(x, t) = \sum_{j=1}^{\infty} A_j X_j(x) \cos(\omega_j t), \quad (41)$$

where  $A_j$ ,  $X_j$  and  $\omega_j$  are the mode coefficients, mode functions and natural frequencies, respectively. These quantities are determined by (Bottega 2006)

$$A_j = \frac{1}{\|X_j\|^2} \int_0^L X_j(x) s_y(x, 0) dx, \quad (42)$$

$$X_j(x) = \cosh(\beta_j x) - \cos(\beta_j x) - \frac{\cosh(\beta_j L) + \cos(\beta_j L)}{\sinh(\beta_j L) + \sin(\beta_j L)} [\sinh(\beta_j x) - \sin(\beta_j x)], \quad (43)$$

$$w_j = \beta_j L \sqrt{EI_{xx}/m^4}, \quad (44)$$

where  $\beta_j L$  are the roots of the characteristic equation  $\cosh(\beta_j L)\cos(\beta_j L) + 1 = 0$  that give non-trivial solutions to the Euler–Bernoulli dynamic beam equation. Figs 3(b) and (c) show the analytical solution expressed by eq. (41) plotted at the end of the beam ( $x = L$ ) for two different starting conditions. In Fig. 3(b) the starting condition is the first mode solution, and in Fig. 3(c) the static solution is used as the starting condition. In both cases, the analytical solutions are plotted together with the results from the classical SPECFEM implementation. These figures show a perfect match between the analytical solution and our implementation of the classical theory for cantilever beam bending.

With the benchmarks in place, we run a simulation using the geometrically non-linear equations and compare the recorded deflections with the classical theory. To further benchmark the results, we implemented the classical and geometrically non-linear

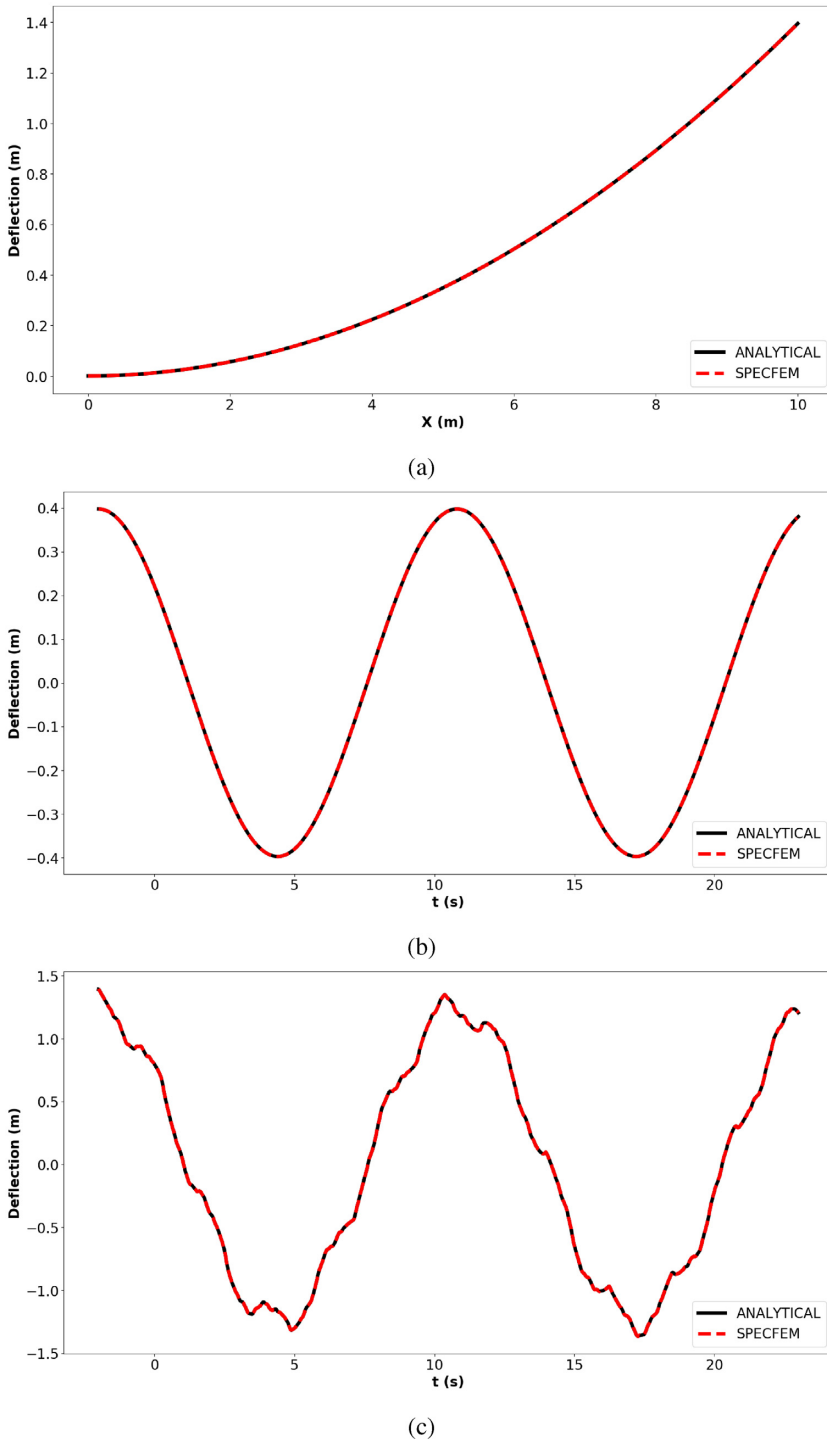


**Figure 3.** Cantilever beam benchmarks comparing the SPECFEM implementation of the classical theory with Euler–Bernoulli beam theory. Panel (a) shows the static solution, and panels (b) and (c) show the dynamic solutions starting from the first mode solution and the static solution, respectively.

equations for the static case (using the Lagrangian strain measure) in FEniCS (Alnaes *et al.* 2015). The static results are plotted in Fig. 4(a), where we see that classical and non-linear results for SPECFEM and FEniCS show almost perfect overlap. We also note that the difference between the classical and the non-linear results are significant, with a 6.45 per cent difference in deflection at the end of the beam. Fig. 4(b) shows the dynamic results, recorded at the end of the beam ( $x = L$ ), where the starting condition is

the non-linear static solution. The difference is plotted in the same figure and is on the order of a few per cent. For this experiment the non-linear implementation takes about three times as long to run as the classical implementation for the static simulation, and about five times as long for the dynamic simulation. This comes down to having to update the boundary conditions for every time step in the static case, and having to compute the strain as a series expansion.

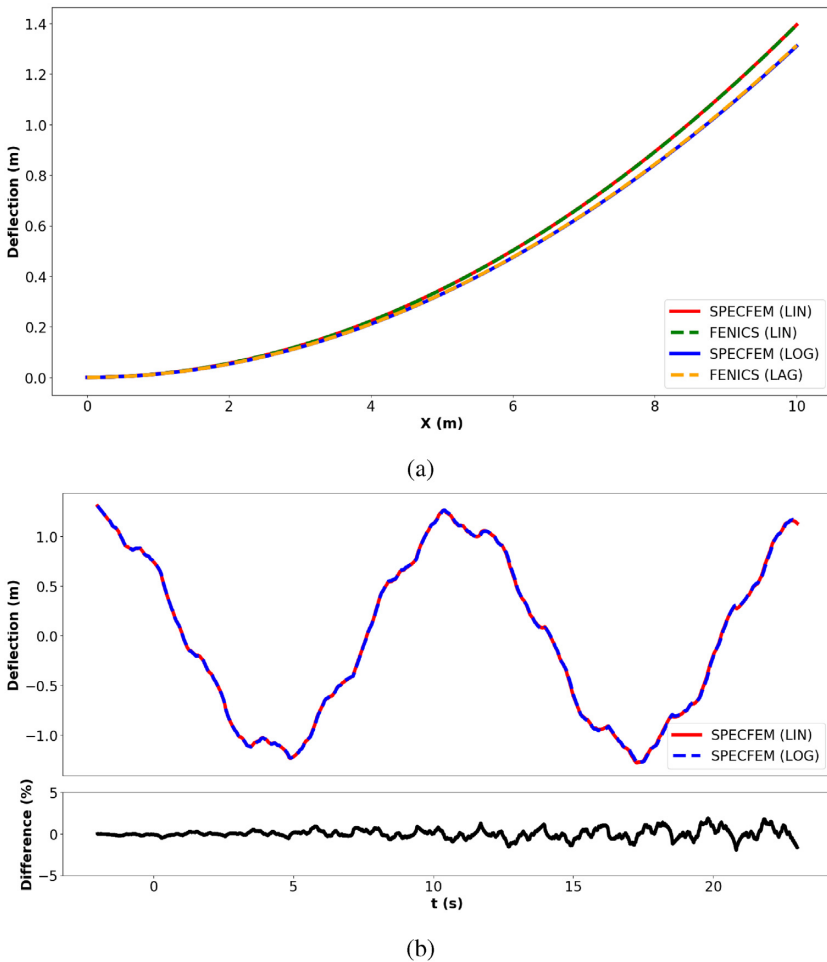


**Figure 4.** Cantilever beam simulations comparing the classical and geometrically non-linear theories. Panel (a) shows the static solution for SPECFEM and FEniCS. Panel (b) shows the dynamic solution for SPECFEM, starting from the static solution, and the difference in percent.

### 3.2 Seismic experiment

We consider a region in Southern California, as shown in Fig. 5, for two elastic models and two source configurations. The model dimensions are  $666 \text{ km} \times 503 \text{ km} \times 60 \text{ km}$ , and the boundary conditions are absorbing (Stacey 1988) on all sides except for the free surface.

The meshes are unstructured and become coarser with increasing depth. The first model has no topography and consists of a 1-D velocity profile, whereas the second model has topography and involves 3-D variations in wave speeds. For this reason the two models have different meshes, but the resolution and number of elements are approximately the same. The first model is the 1-D Southern California model (Kanamori & Hadley 1975; Dreger & Helmberg 1990; Wald *et al.* 1995), which has compressional and shear wave speed profiles as shown in Fig. 6(a). It is composed of 1 105 920 spectral elements, and each element has 5 GLL points in each direction, resulting in 74 242 880 degrees of freedom. The largest element size in the model is 9.3 km while the smallest element size is 1.3 km. The second model is a 3-D Southern California model (Tape *et al.* 2009), which has the shear wave speed distribution shown in Fig. 6(b). This model consists of 902 880 spectral elements, and, with the same number of GLL points per element, this gives 61 288 276 degree of freedom. The largest element size in the model is 20.6 km and the smallest element size is 0.5 km. It

is worth noting that the smallest wave speeds in the 3-D model are significantly lower than in the 1-D model, while the largest wave speeds are approximately the same for both models. The highest frequency resolved by the models is of order 0.1 Hz.

For each model we use two different source configurations, for a total of four simulations. The first source is a point source representation of the 1994 Northridge earthquake (Field *et al.* 1998) with a Gaussian source time function, a half duration of 5.4 s, and an onset time  $t_0 = 8.2$  s. The source represents a blind thrust event of magnitude  $M_w = 6.7$  at a depth of 16.8 km. The second source is the finite source used in Krishnan *et al.* (2006), mapping a 2002 earthquake on the Denali fault system (Eberhart-Phillips *et al.* 2003) onto the San Andreas fault. The rupture starts at the northern end of the fault and propagates in a southeasterly direction for a total of about 290 km. The source is represented as a collection of 45 240 point sources evenly distributed along the San Andreas fault. Each source has a Gaussian source time function, with half durations ranging from 0.4 to 6.0 s, and the onset times are in the range  $t_0 = 0.0\text{--}100.0$  s. The source represents a strike-slip event of magnitude  $M_w = 7.9$  at depths less than 10 km.

For all simulations we use a timestep of  $\Delta t = 5.0$  ms and we run the simulations for 200 s. We record the three components of displacement at each timestep for every point in the model. In order to compare the simulation results with the classical theory, we also

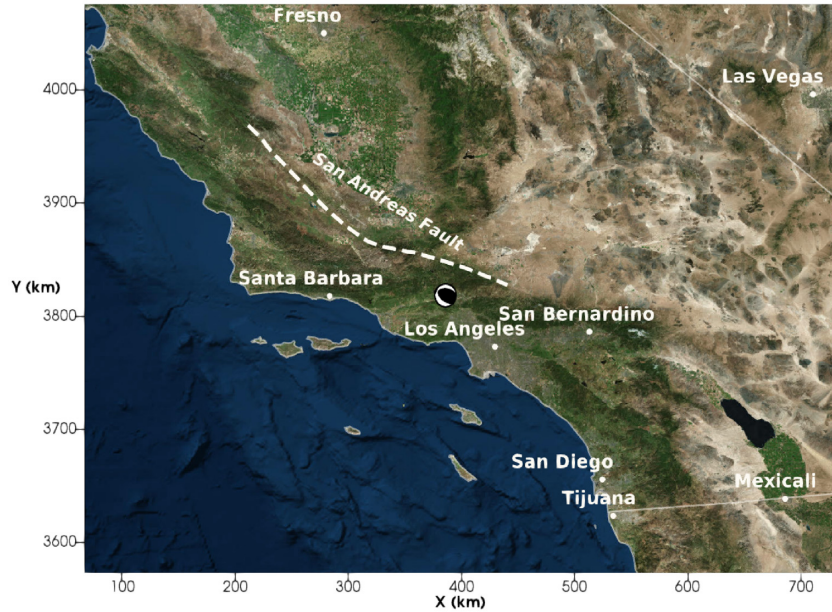


**Figure 5.** Map view of the Southern California region with two source configurations. The point source is shown as a beach ball, and the finite source as a dashed, white line.

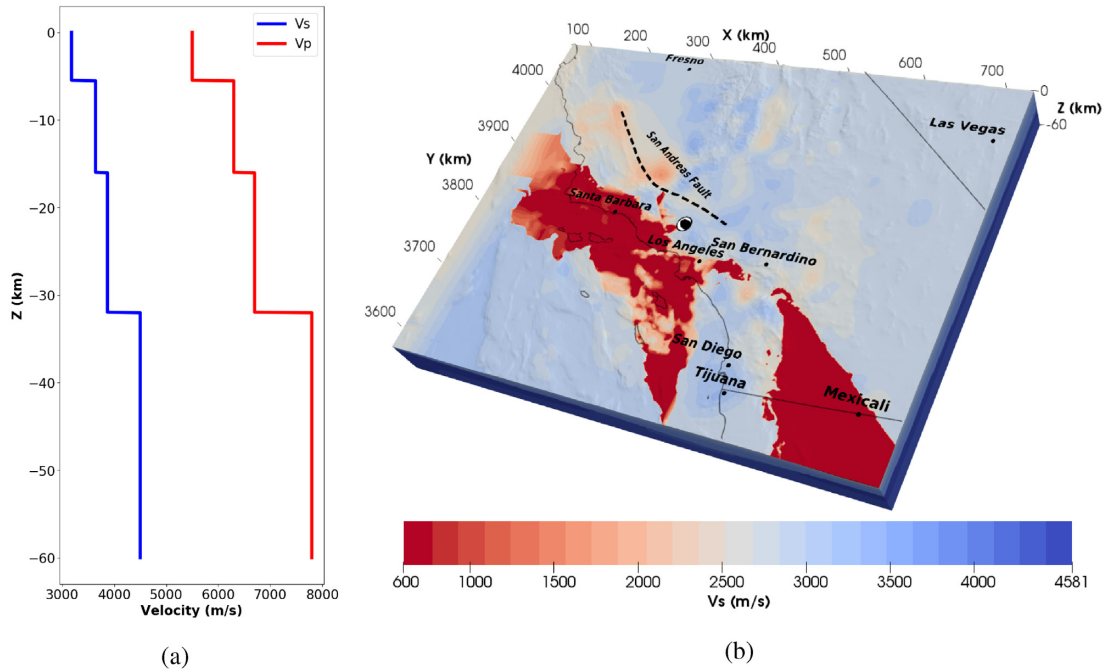


**Figure 6.** Velocity model of Southern California: (a) 1-D shear and compressional wave speed profiles, (b) 3-D shear wave speed model.

run the simulations with an SEM implementation of the classical theory. To ensure that the two simulations are driven by the exact same source, in both simulations we use the infinitesimal strain measure in spectral elements where the source is located. To get a better sense of the differences between the results, we compute the following measure for every point in the model:

$$\Delta(x) = \frac{1}{2} \log \left[ \frac{\int s_l^2(x, t) dt}{\int s_n^2(x, t) dt} \right]. \quad (45)$$

Here  $s_l$  denotes the norm of the displacement field recorded in the simulations using the classical (linear) formulation and  $s_n$  the norm of the displacement field recorded in the simulations using the general (geometrically non-linear) formulation. The results are shown in Fig. 7, where the measure is plotted in percent ( $100 \cdot \Delta$ ) on the surface. The results show that the differences are similar for the 3-D model simulations and the 1-D model simulations, but they are larger with the finite source configuration than with the point source configuration. We note, however, that even for the finite

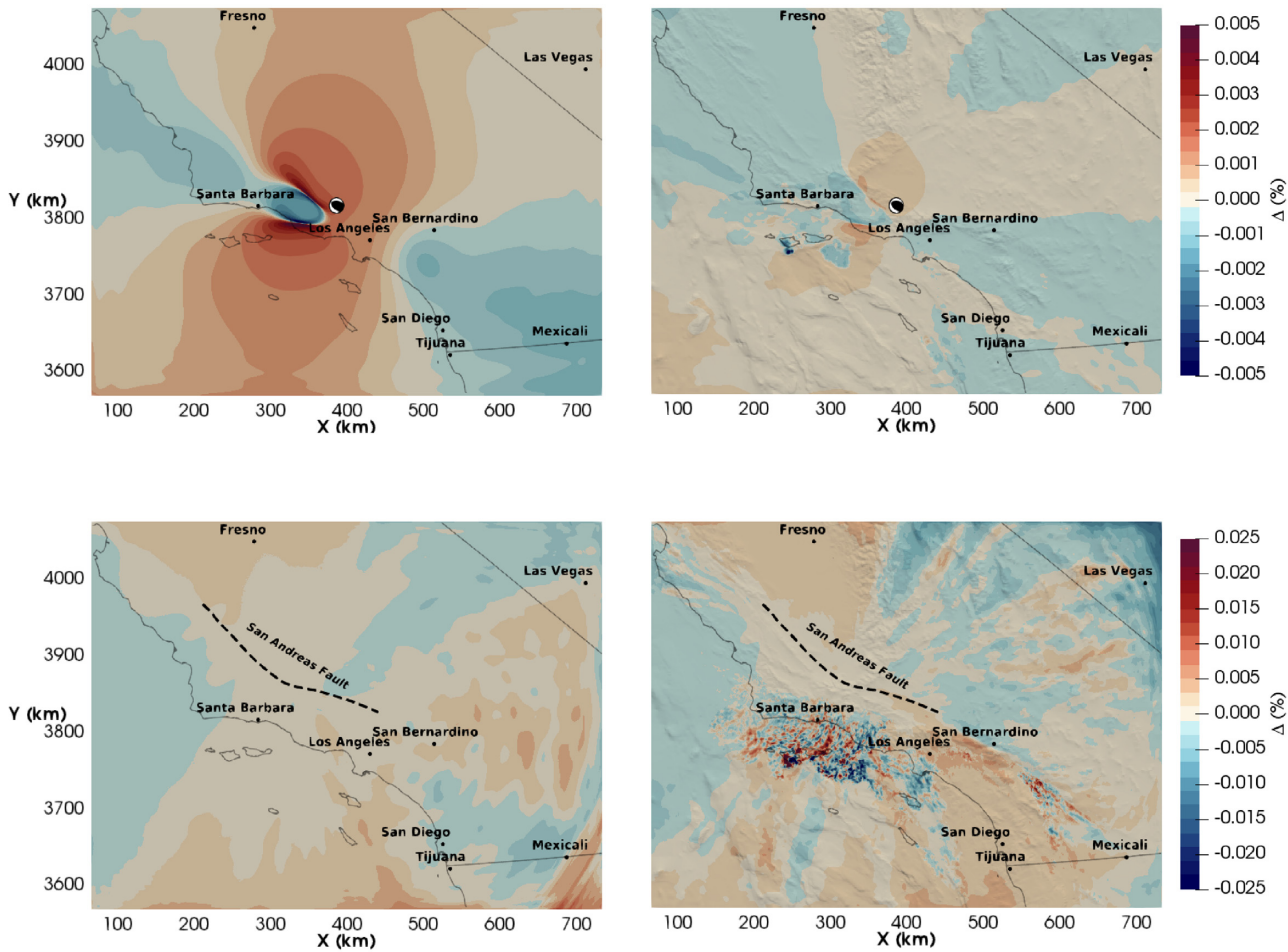


**Figure 7.** Surface view of differences between the classical (linear) and general theories according to eq. (45) for four simulations: Left-hand panel 1-D model. Right-hand panel: 3-D model. Top panel: point source. Bottom panel: finite source. Note that the results are plotted in percent ( $100 \cdot \Delta$ ).

source simulations, the largest difference in the entire volume is about 0.1 per cent, which is insignificant.

This experiment suggests that the effect of solving the geometrically non-linear equations is minor for wave propagation in an isotropic elastic medium. This result is not surprising, since observed displacements in seismology are commonly small, which makes the linearized, classical theory a good approximation for this application. For the single source simulation, the non-linear implementation takes about three times longer than the classical implementation. This is because the boundary conditions and the source must be updated with the deformation gradient for every timestep. This is only done in the mesh partitions that contain the source and along the boundary, respectively, which means that the non-linear implementation is more poorly load balanced. The performance can be greatly improved by accounting for this additional work in the load balancing. Since our intention here is to provide a proof of concept, we have omitted this optimization for now. For every element in the model there is also some cost associated with having to compute the strain as a series expansion. The workload imbalance is more pronounced in the finite source simulations since it is represented by 45 240 point sources. This causes the mesh partitions that contain the source to have much more work for each time step than the partitions that do not contain the source. For this reason, the non-linear implementation takes about 15 times longer than the classical implementation for the finite source simulations.

## 4 CONCLUSIONS

We have shown that the equation of motion governing seismic wave propagation can be written in a Lagrangian framework in such a way that its weak form is analogous to the weak form of the linearized equation of motion. The added complexity is that we need to track the deformation gradient. Tracking the deformation gradient enables us to express all the relevant quantities in terms of the reference domain, and it allows us to introduce the logarithmic strain measure into our formulation. This makes it a geometrically non-linear formulation, where we make no assumption about the size of deformation.

Our numerical experiments show that the effect of solving the geometrically non-linear equations can be significant in cases where finite deformation occurs, such as cantilever beam bending. In cases where the deformations are smaller, such as for seismic wave propagation, the results are similar to solving the classical equations. However, since the formulations are nearly the same, we might as well solve the geometrically non-linear equations. The geometrically non-linear implementation is found to take about three times as long to run compared to the classical implementation. This could potentially be improved by properly load balancing the geometrically non-linear implementation.

We have not considered material non-linearities in this work, but these could be incorporated in the constitutive relation. In

seismology, non-linear effects are often tied to the material. An example is soil amplification in weak and strong motion, where non-linear effects are observed as sediments begin to yield beyond a certain level of strain. This type of material behaviour violates Hooke's law, which suggests that it is necessary to use a more sophisticated constitutive relation in such cases. Therefore, one might expect that extending our geometrically non-linear formulation to capture some degree of material non-linearity could lead to larger differences in our seismic numerical experiment, especially in low-wavespeed sedimentary basins close to the surface, where material non-linearities would be most significant.

## ACKNOWLEDGEMENTS

This paper was inspired by conversations with the late Albert Tarantola. Albert deeply believed deformation should be captured in terms of the logarithmic strain, and was a strong advocate for solving the proper laws of physics whenever possible. We thank Carl Tape for providing the model and mesh for the 3-D Southern California model and Swaminathan Krishnan for providing the CMT solution for the finite seismic source. We thank Yann Capdeville and an anonymous reviewer for comments and suggestions which helped to improve the manuscript. This research used resources provided by the Princeton Institute for Computational Science & Engineering (PICSciE). 3D data were visualized using the open-source parallel visualization software ParaView/VTK ([www.paraview.org](http://www.paraview.org)). The open source spectral-element software package SPECFEM3D used for this article is freely available via the Computational Infrastructure for Geodynamics (CIG; [geodynamics.org](http://geodynamics.org)). This research was supported by NSF grant 1644826.

## REFERENCES

- Aki, K., 1968. Seismic displacements near a fault, *J. geophys. Res.*, **73**, 5359–5376.
- Aki, K., 1993. Local site effects on weak and strong ground motion, *Tectonophysics*, **218**, 93–111.
- Alnaes, M.S. *et al.*, 2015. The fenics project version 1.5, *Arch. Numer. Software*, **3**(100), 9–23.
- Beresnev, I.A. & Wen, K.L., 1996. Nonlinear soil response—a reality? *Bull. seism. Soc. Am.*, **86**(6), 1964–1978.
- Bottega, W.J., 2006. *Engineering Vibrations*, 1st edn, CRC Press.
- Chang, C.-Y.M.C. & Tang, H.T., 1996. Inference of dynamic shear modulus from lotung downhole data, *J. Geotech. Eng.*, **122**(8), 657–665.
- Dahlen, F.A. & Tromp, J., 1998. *Theoretical Global Seismology*, Princeton University Press.
- Dreger, D.S. & Helmberg, D.V., 1990. Broadband modeling of local earthquakes, *Bull. seism. Soc. Am.*, **80**(5), 1162–1179.
- Eberhart-Phillips, D. *et al.*, 2003. The 2002 Denali fault earthquake, Alaska: a large magnitude, slip-partitioned event, *Science*, **300**(5622), 1113–1118.
- Elgamal, A.-W., Zeghal, M., Tang, H.T. & Stepp, J.C., 1995. Lotung down-hole array. I: evaluation of site dynamic properties, *J. Geotech. Eng.*, **121**(4), 350–362.
- Field, E.D., Johnson, P.A., Beresnev, I.A. & Zeng, Y., 1997. Nonlinear ground-motion amplification by sediments during the 1994 Northridge earthquake, *Seismol. Res. Lett.*, **390**, 599–602.
- Field, E.D. *et al.*, 1998. Nonlinear site response: where we're at (a report from a SCEC/peer seminar and workshop), *Seismol. Res. Lett.*, **69**(3), 230–234.
- Gere, J.M. & Goodno, B.J., 2008. *Mechanics of Materials*, 7th edn, Cengage Learning.
- Hardin, B.O. & Drnevich, V.P., 1972. Shear modulus and damping in soils: design equations and curves, *Proc. Am. Soc. Civil Eng. J. Soil Mech. Found. Div.*, **98**, 667–692.
- Heaton, T.H., 1990. Evidence for and implications of self-healing pulses of slip in earthquake rupture, *Phys. Earth planet. Inter.*, **64**, 1–20.
- Hencky, H., 1928. Über die form des elastizitätsgesetzes bei ideal elastischen stoffen, *Zeitschrift für technische Physik*, **9**, 215–220.
- Ichimura, T. *et al.*, 2015. Implicit nonlinear wave simulation with 1.08t dof and 0.270t unstructured finite elements to enhance comprehensive earthquake simulation, in *Proceedings of the International Conference for High Performance Computing, Networking, Storage and Analysis, SC '15*, pp. 4:1–4:12, ACM, New York, NY, USA.
- Kanamori, H. & Hadley, D., 1975. Crustal structure and temporal velocity change in Southern California, *Pure appl. Geophys.*, **113**, 257–280.
- Komatitsch, D. & Tromp, J., 1999. Introduction to the spectral element method for three-dimensional seismic wave propagation, *Geophys. J. Int.*, **139**(3), 806–822.
- Komatitsch, D. & Tromp, J., 2002a. Spectral-element simulations of global seismic wave propagation – I. Validation, *Geophys. J. Int.*, **149**(2), 390–412.
- Komatitsch, D. & Tromp, J., 2002b. Spectral-element simulations of global seismic wave propagation – II. Three-dimensional models, oceans, rotation and self-gravitation, *Geophys. J. Int.*, **150**(1), 303–318.
- Komatitsch, D. & Villette, J.-P., 1998. The spectral element method: an efficient tool to simulate the seismic response of 2D and 3D geological structures, *Bull. seism. Soc. Am.*, **88**(2), 368–392.
- Komatitsch, D. *et al.*, 2012. *Specfem3d cartesian v2.0.2*.
- Krishnan, S., Ji, C., Komatitsch, D. & Tromp, J., 2006. Case studies of damage to tall steel moment-frame buildings in Southern California during large San Andreas earthquakes, *Bull. seism. Soc. Am.*, **96**(4A), 1523–1537.
- Miller, K., Joldes, G., Lance, D. & Wittek, A., 2007. Total lagrangian explicit dynamics finite element algorithm for computing soft tissue deformation, *Commun. Numer. Methods Eng.*, **23**(2), 121–134.
- Novozhilov, V.V., 1999. *Foundations of the Nonlinear Theory of Elasticity*, Dover Publications.
- Pavlenko, O.V., 2001. Nonlinear seismic effects in soils: numerical simulation and study, *Bull. seism. Soc. Am.*, **91**(2), 381–396.
- Peter, D. *et al.*, 2011. Forward and adjoint simulations of seismic wave propagation on unstructured hexahedral meshes, *Geophys. J. Int.*, **186**, 721–739.
- Stacey, R., 1988. Improved transparent boundary formulations for the elastic-wave equation, *Bull. seism. Soc. Am.*, **78**(6), 2089–2097.
- Tape, C., Liu, Q., Maggi, A. & Tromp, J., 2009. Adjoint tomography of the Southern California crust, *Science*, **325**, 988–992.
- Tarantola, A., 2005. *Elements for Physics*, Springer.
- Wald, L.A., Hutton, L.K. & Given, D.D., 1995. The Southern California network bulletin: 1990–1993 summary, *Seism. Res. Lett.*, **66**, 9–19.
- Wood, R.D. & Zienkiewicz, O.C., 1977. Geometrically nonlinear finite element analysis of beams, frames, arches and axisymmetric shells, *Comput. Struct.*, **7**(6), 725–735.
- Zeghal, M., Elgamal, A.-W., Tang, H.T. & Stepp, J.C., 1995. Lotung down-hole array. II: evaluation of soil nonlinear properties, *J. Geotech. Eng.*, **121**(4), 363–378.
- Zienkiewicz, O., Taylor, R.L. & Zhu, J.Z., 2013. *The Finite Element Method: Its Basis and Fundamentals*, 7th edn, Butterworth-Heinemann.
- Zienkiewicz, O., Taylor, R.L. & Fox, D.D., 2014. *The Finite Element Method for Solid and Structural Mechanics*, 7th edn, Butterworth-Heinemann.